



Contents lists available at ScienceDirect

Engineering Science and Technology, an International Journal

journal homepage: www.elsevier.com/locate/jestch

Modeling and analysis of the leakage performance of the spherical valve plate pair in axial piston pumps

Haoqin Ma^a, Wei Liu^b, Dongwei Wu^c, Haomin Shan^a, Shiqi Xia^{a,*}, Yimin Xia^a^a College of Mechanical and Electrical Engineering, Central South University, No.932 South Lushan Road, Changsha 410083, China^b China Railway Construction Heavy Industry Corporation Limited, No.88, Donggi Road, National Economic & Technical Development Zone, Changsha 410100, China^c Weichai Power Corporation Limited, 197 A, Fushou East Street, High-Tech Development Zone, Weifang 261061, China

ARTICLE INFO

ABSTRACT

Keywords:

Large displacement pumps
Spherical valve plate pair
Oil film
Leakage
Modeling

Axial piston pumps are widely used in construction machinery due to the high power density. The leakage performance of the spherical valve plate pair is of great significance to the large displacement pumps' volumetric efficiency. However, the model and calculation of leakage are unclear. This paper proposed a cylinder block dynamic and oil film lubrication based leakage model of the spherical valve plate pair for axial piston pumps. Numerical solutions on the leakage performance under different working conditions were carried out. The tilt behavior of the cylinder block, thickness, and longitude velocity of the oil film were solved. In addition, the effects of central spring stiffness on leakage performance were analyzed and experiments were conducted. Results show that the pump is with poor volumetric efficiency for operation at low speed and high pressure, and $\pm 5\%$ adjustment of spring stiffness leads to a 237% maximum leakage gap for spherical valve plate pair.

1. Introduction

Axial piston pump has been widely used as a power component in industrial hydraulic systems, it features a compact structure, high efficiency, and continuously adjustable output [1]. The key to the efficient operation of piston pumps is the oil film that forms between the three pairs of relatively movable components (valve plate pair, piston pair, slipper pair) to separate each other in the pump [2–4]. The undersized or oversized oil film will cause metal-to-metal contact and leakage increase, respectively [5,6]. The oil film characteristics of friction pair are one of the critical design issues for pumps. In general, the valve plate pair has the largest contact area among the three friction pairs [7], and the high-speed rotating cylinder block has extremely complex dynamic behavior [8]. The failure of the valve plate pair is one major cause of pump function degradation [9], so this paper focuses on the valve plate pair's oil film characteristics. The oil film characteristics can be described by leakage, carrying capacity, and mechanical efficiency, of which leakage is the easiest to detect.

Leakage performance research on the valve plate pair mainly consists of theoretical and experimental investigations. In terms of theory, oil film lubrication models can be divided into two main categories based on the consideration of hydrodynamic effects or not. The first category is

a hydrostatic model [10,11] that uses empirical formulas, which is a simple and effective way to evaluate the carrying capacity of interfaces, from which the current design method for valve plate pairs "Surplus Pressing Force" [7] is derived. The hydrodynamic model is the basis of the second category, which accounts for hydrodynamic effects and features the oil film characteristics by the Reynolds equation [12,13]. The Reynolds equation is a partial differential equation [14] and can only be solved by numerical methods, such as finite element method (FEM) [15], finite volume method (FVM) [16], finite difference method (FDM) [17,18]. The high pressure and speed friction interface leads to elastic micro-deformation and thermal rise of the structure, to which the oil film is strongly sensitive [19]. The elastohydrodynamic model [20–22] is derived by applying a structural deformation solution to the hydrodynamic model, on top of which the thermal elastohydrodynamic model [23–26] is developed when considering the interface energy transfer. With the increase in model accuracy, the computational difficulty and effort increase rapidly, the rational optimization of solver also becomes research [27]. Experimental investigations serve as essential means to investigate the operation of valve plate pairs and to assess the reliability of theoretical models. Research shows that the major reason for leakage is the uneven carrying of the lubrication interface [28], which forms an observable wedge-shaped oil film [29,30]. Other researchers have investigated cylinder block tilt behavior [28,31–33], as

* Corresponding author.

E-mail addresses: mahaoqin@csu.edu.cn (H. Ma), lw2002cn2000@163.com (W. Liu), wudongwei@weichai.com (D. Wu), CSU_SHM@csu.edu.cn (H. Shan), shiqixia@csu.edu.cn (S. Xia), xiaymj@csu.edu.cn (Y. Xia).<https://doi.org/10.1016/j.jestch.2023.101498>

Received 30 March 2023; Received in revised form 3 July 2023; Accepted 23 July 2023

Available online 3 August 2023

2215-0986/© 2023 Karabuk University. Publishing services by Elsevier B.V. This is an open access article under the CC BY-NC-ND license (<http://creativecommons.org/licenses/by-nc-nd/4.0/>).

Nomenclature	
A	the ball center of the piston head
a	acceleration
B	the circle center at the bottom of piston
B'	pressure action point in the piston chamber
C	a constant of the equation
d	distance from a point to the y-axis
e	the offset of the piston path from the IDC pitch circle
F	force
H	the piston remaining stroke
h	oil film thickness
K	spring stiffness
l	spatial distance
L	moment arm
M	piston-slipper assembly center of mass
N	number of pistons
n	pump rotation speed
p	oil pressure
Q	total leakage
q	spherical valve plate pair leakage
r	distance from a point to the z-axis
S	the piston stroke
v	velocity
α	inclination of piston
β	inclination of swashplate
δ	gap of spherical valve plate pair
ϵ	pressure iteration error
θ	longitude direction
μ	dynamic viscosity
ρ	oil density
τ	shear stress
φ	the angle of rotation
ω	angular velocity
O-X, Y, Z	cylinder block coordinate system
O'-X', Y', Z'	swashplate coordinate system
$o-x, y, z$	fluid coordinate system
$o-R, \theta, \varphi$	spherical coordinate system
Subscript	
a	axial
azi	tilt azimuth
c	Coriolis
cy	cylinder block
inner	inner sealing area
N	normal to the swashplate
oil	oil film
outer	outer sealing area
p	pressure
pi	piston
p-s	piston-slipper assembly
r	radial
sc	spline coupling
sp	spring
tilt	tilt angle
vp	valve plate
0	IDC Point
_X/ Y/ Z	Component in X (or Y or Z) direction

the behaviour directly reflects the mechanical equilibrium of friction interface.

The aforesaid study primarily focuses on a classical axial piston pump. With the broader utilization of hydraulic systems, axial piston pumps have been put forward with increasingly complex demands. For example, the enormous burden and harsh geological conditions of tunnel boring machines (TBM) dictate a pump with a targeted design for large displacement ($\geq 750 \text{ mL/r}$) and high pressure ($\geq 35 \text{ MPa}$) [34]. There is a dilemma of selection while attempting to enlarge the displacement of piston pumps, i.e., an increase in displacement generally means an increase in the size of structure, which is unacceptable for the limited pump internal space. As shown in Fig. 1, a large displacement (750 mL/r) axial piston pump with the spherical valve plate pair (SVPP) is used to tackle the dilemma, and the SVPP consists of a conical cylinder block (CCB) and a spherical valve plate (SVP). The pump with SVPP operates identically to classical piston pumps, but the inclined piston allows a larger reciprocating stroke, and the reduced size of SVP permits higher pump speeds. In practice, the SVPP structure designed by

“Surplus Pressing Force” is hard to meet the pump’s volumetric efficiency demands, so the central spring preload for each pump is adjusted according to the leakage performance.

Documents of SVPP are scarce and the research is fragmented. Barth’s team carried out an early study of the dynamics [35,36] and triangular grooves [37] of the SVPP with hydrostatic models [38], and the accuracy of the model requires improvement. They further researched the control performance [39,40] and vibration characteristics [41] of the pump. Shi et al. [42] completed a kinematic analysis of the rotating assembly inside the pump, and the simulation gave flow fluctuations, but the leakage and mechanical properties were not considered. Li et al. [43] studied the piston flow characteristics by a discrete hydrostatic model. Chen et al. [44] calculated a leakage between the slipper and swashplate in the pump with SVPP but lacked experimental validation. Zhao et al. [45] used CFD software to simulate the submerged cavitation jet in the unloading groove, of which the theoretical analysis is absent.

In conclusion, the leakage performance of valve plate pairs depends on kinematic characteristics, oil film lubrication performance, and

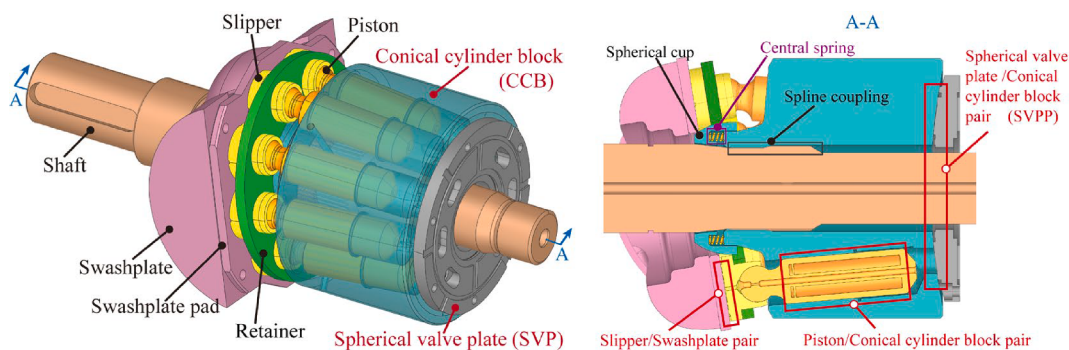


Fig. 1. Diagrams of 750 mL/r axial piston pumps.

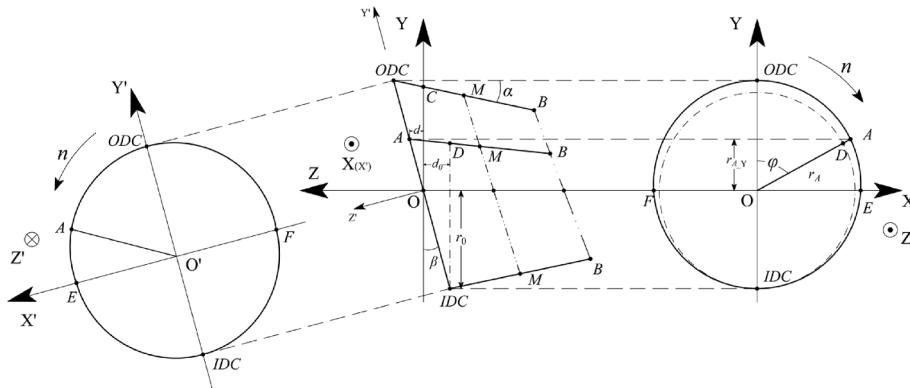


Fig. 2. Diagram of piston-slipper assembly macro motion.

dynamic effects. The study of SVPP remains many limitations, which include the following challenging problems:

- (1) the spatial posture and dynamics of SVPP are further complicated by the fact that a spherical oil film cannot be reduced to a 2D planar fluid flow issue like a wedge-shaped oil film. Research on oil film lubrication and the complex dynamic behavior of SVPP is blank.
- (2) the assessment of SVPP leakage is mainly based on empirical formulas of hydrostatics and the results have significant limitations and errors.
- (3) the parametric study of SVPP impact on oil film leakage performance is scarce, particularly for central spring stiffness. Previous work has failed to guide the design and fabrication of 750 mL/r pumps.

This study aims to obtain the leakage performance of the SVPP in axial piston pumps, specifically for a 750 mL/r pump. In response to the limitations of the current study, the main work of this paper is summarized as follows:

- (1) a kinematic and dynamic model of SVPP was established, the equations for the spherical oil film lubrication characteristics were derived and solved by numerical methods, resulting in an accurate leakage model;
- (2) the effect of load pressure and speed on the SVPP leakage was investigated, and the mechanical causes of the leakage variation with work conditions were discussed with the support of established theoretical models;
- (3) experiments were carried out on a 750 mL/r axial piston pump, with a focus on the effect of central spring stiffness on leakage. A comparison of the experiment and simulation results qualitatively verifies the model's validity.

The remainder of this paper is arranged as follows: Section 2 established a leakage calculation model for SVPP; Section 3 derives the numerical results of the leakage model and conducts a parametric analysis; Section 4 is a pump test to verify the accuracy of the leakage model. Summary and Conclusions are presented in Section 5. This study helps to understand the leakage performance of SVPP and assists in the parameters design, which is of great significance.

2. Mathematical modeling

Leakage is usually described by flow loss. The leakage of SVPP depends on the area of the gap interface and the velocity of fluid. Both are related to oil film geometry and lubrication characteristics, which in turn are influenced by the dynamic characteristics of components. Therefore, a detailed dynamic analysis must be carried out for SVPP.

2.1. Dynamic model

To derive the forces on the SVPP motion components, a description of the piston-slipper assembly kinematics is required. Fig. 2 shows the macro motion of piston-slipper assembly, with two right-angle coordinate systems defined. The (X, Y, Z) is the cylinder block coordinate system and the (X', Y', Z') is the swashplate coordinate system, which has a common origin. The origin is located at the intersection between the axis of the shaft and the special plane containing the centers of all piston heads. The Z-axis is consistent with the axis of the shaft, the Y-axis is selected upward direction to be positive, and the positive direction of the X-axis is established by the right-hand rule. The X'Y' plane is parallel to the swashplate, and Z' is perpendicular to the swashplate surface and points outward. In Fig. 2, ODC indicates an outer dead center where the piston head reaches the maximum distance from the CCB bottom, and IDC indicates an inner dead center where the piston head reaches the minimum distance from the CCB bottom.

As shown in Fig. 2, the piston head rotates clockwise in the XY plane with speed n . The partial motion and projection relationship is expressed as:

$$\begin{cases} \frac{d_0}{r_0} = \frac{d}{r_{A,Y}} = \tan\beta \\ r_{A,Y} = r_A \cos\varphi = (r_0 + e) \cos\varphi \\ \frac{e}{d + d_0} = \tan\alpha \end{cases} \quad (1)$$

A joint solution gives:

$$d = \frac{r_0 \tan\beta \cos\varphi (1 + \tan\alpha \tan\beta)}{1 - \tan\alpha \tan\beta \cos\varphi} \quad (2)$$

The remaining stroke of the piston in the CCB bore can be deduced as:

$$H = \frac{d + d_0}{\cos\alpha} = \frac{r_0 \tan\beta (1 + \cos\varphi)}{\cos\alpha (1 - \tan\alpha \tan\beta \cos\varphi)} \quad (3)$$

When the angle of rotation is zero, the piston stroke is maximum:

$$H_{\max} = \frac{2r_0 \tan\beta}{\cos\alpha (1 - \tan\alpha \tan\beta)} \quad (4)$$

The expression for the piston stroke can be given as:

$$S_{p-s} = H_{\max} - H = \frac{r_0 \tan\beta (1 - \cos\varphi) (1 + \tan\alpha \tan\beta)}{\cos\alpha (1 - \tan\alpha \tan\beta) (1 - \tan\alpha \tan\beta \cos\varphi)} \quad (5)$$

The axial velocity and axial acceleration of the piston are obtained by differentiating Eq. (5) in sequence:

$$v_{p-s} = \frac{dS_{p-s}}{dt} = \frac{r_0 \tan\beta \sin\varphi (1 + \tan\alpha \tan\beta) \omega}{\cos\alpha (1 - \tan\alpha \tan\beta \cos\varphi)^2} \quad (6)$$

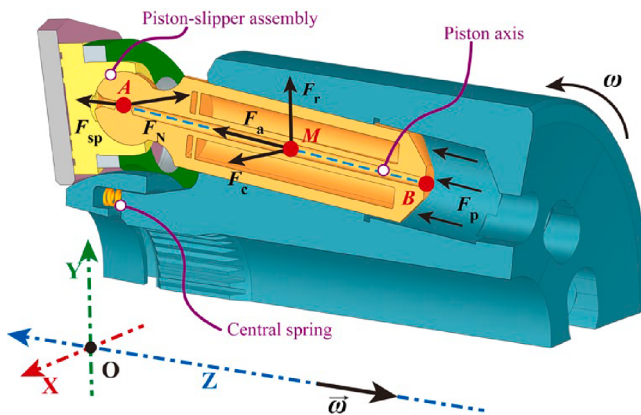


Fig. 3. Force analysis of piston-slipper assembly.

$$\begin{aligned} a_{p-s} &= \frac{dv_{p-s}}{dt} \\ &= [r_0 \tan \beta (1 + \tan \alpha \tan \beta) (\cos \varphi - \tan \alpha \tan \beta \cos^2 \varphi \\ &\quad - 2 \tan \alpha \tan \beta \sin^2 \varphi) \omega^2] / [\cos \alpha (1 - \tan \alpha \tan \beta \cos \varphi)^3] \end{aligned} \quad (7)$$

Fig. 3 illustrates the forces acting on the piston-slipper assembly. Specifically, these include the axial inertia force (F_a), the radial inertia force (F_r), the Coriolis inertia force (F_c), the central spring force (F_{sp}), and the swashplate reaction force (F_N). Frictional forces with small values are neglected to simplify the analysis.

F_a , F_r , and F_c belong to the inertial forces, which all act on the center of mass (M). The spatial coordinates of M and the equations of each inertial force above can be expressed in matrix form:

$$L_M = [(r_0 + e - l_{AM} \sin \alpha) \sin \varphi \quad (r_0 + e - l_{AM} \sin \alpha) \cos \varphi \quad Z_A - l_{AM} \cos \alpha] \quad (8)$$

$$F_a = [m_{p-s} a_{p-s} \sin \alpha \sin \varphi \quad m_{p-s} a_{p-s} \sin \alpha \cos \varphi \quad m_{p-s} a_{p-s} \cos \alpha] \quad (9)$$

$$F_r = [m_{p-s} \omega^2 L_{M-X} \quad m_{p-s} \omega^2 L_{M-Y} \quad 0] \quad (10)$$

Which, the Coriolis acceleration and Coriolis inertia force need to be obtained through Eq. (6):

$$a_c = 2\omega \times v_{p-s} = \begin{cases} 2\omega v_{p-s} \sin(\pi - \alpha) & 0 \leq \varphi < \pi \\ 2\omega v_{p-s} \sin \alpha & \pi \leq \varphi < 2\pi \end{cases} \quad (11)$$

$$F_c = [m_{p-s} a_c \cos \varphi \quad m_{p-s} a_c \cos \varphi \quad 0] \quad (12)$$

F_p , F_{sp} , and F_N belong to non-inertial forces. Specifically, F_p acts at the piston bottom, and the direction is along its axis. For the convenience of the solution, the force is concentrated at point B. The matrix expression of the force and force arm is as follows:

$$F_p = [\pi r_{pi}^2 p \sin \alpha \sin \varphi \quad \pi r_{pi}^2 p \sin \alpha \cos \varphi \quad \pi r_{pi}^2 p \cos \alpha] \quad (13)$$

$$L_B = [(r_0 + e - l_{AB} \sin \alpha) \sin \varphi \quad (r_0 + e - l_{AB} \sin \alpha) \cos \varphi \quad Z_A - l_{AB} \cos \alpha] \quad (14)$$

The spring force (F_{sp}) on the piston-slipper assembly is applied at point A, and the direction of action is along the +Z axis.

$$F_{sp} = \left[0 \quad 0 \quad \frac{l_{sp} K}{N} \right] \quad (15)$$

$$L_A = [(r_0 + e) \sin \varphi \quad (r_0 + e) \cos \varphi \quad Z_A] \quad (16)$$

Under the action of F_p , F_{sp} , and F_a , the piston-slipper assembly squeezes the swashplate, and the swashplate generates the support reaction force (F_N). The Z-component force of F_N cancels with the above three forces, according to which the specific expression can be found. The reaction point of F_N is A.

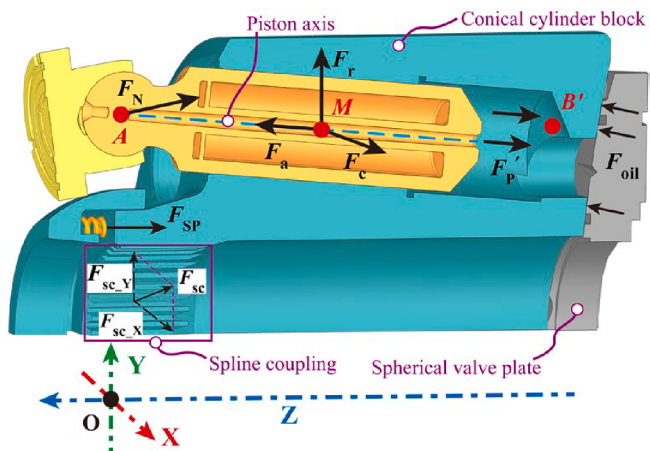


Fig. 4. Force analysis of CCB.

$$F_{N-Z} = (F_p + F_a) \cos \alpha + \frac{F_{sp}}{N} \quad (17)$$

$$F_N = [0 \quad F_{N-Z} \tan \beta \quad F_{N-Z}] \quad (18)$$

Fig. 4 shows the force analysis of CCB. The forces acting on the piston-slipper assembly are transmitted to the cylinder block by solid contact or pressurized oil. Especially, the area of action of CCB subjected to oil pressure F_p' differs from that of the piston. In addition, the CCB is also subjected to the support reaction force provided by the shaft spline and oil film of SVP.

Suppose the area of CCBs' piston bore is A_0 , and the pressure force of individual piston chamber oil applied to CCB is:

$$F_p' = [0 \quad 0 \quad A_0 p] \quad (19)$$

$$L_{B'} = [r_{cy} \sin \varphi \quad r_{cy} \cos \varphi \quad Z_{cy}] \quad (20)$$

According to the above analysis process, the force balance equation and the moment balance equation of the CCB may be written as:

$$\begin{cases} \sum F_X = \sum_{i=1}^N (F_{a,X} + F_{r,X} + F_{c,X}) + F_{sc,X} \\ \sum F_Y = \sum_{i=1}^N (F_{a,Y} + F_{r,Y} + F_{c,Y} + F_{N,Y}) + F_{sc,Y} \\ \sum F_Z = \sum_{i=1}^N F_p' + F_{sp} + F_{oil} \end{cases} \quad (21)$$

$$\begin{cases} \sum M_X = \sum_{i=1}^N [Y_B F_{p,Z} - Z_M (F_{a,Y} + F_{r,Y} + F_{c,Y}) - Z_A F_{N,Y}] + \sum M_{oil,X} \\ \sum M_Y = \sum_{i=1}^N [Z_M (F_{a,X} + F_{r,X} + F_{c,X}) - X_p F_{p,Z}] + \sum M_{oil,Y} \\ \sum M_Z = \sum_{i=1}^N [X_M (F_{a,Y} + F_{r,Y} + F_{c,Y}) - Y_M (F_{a,X} + F_{r,X} + F_{c,X}) + Y_A F_{N,Y}] \end{cases} \quad (22)$$

Eq. (21) shows that the unbalanced forces of CCB in the X and Y-axis are offset by the shaft splines. The CCB in the Z-axis relies on a balance between the oil pressure in the piston chamber, the oil film carrying force and the central spring force, which determines the lubrication state of the oil film. The oil pressure and the oil film carrying force are a pair of mutually canceling hydraulic forces. Normally, the oil film reaction force is slightly greater than the piston chamber pressure, causing the oil film to push the CCB away from the SVP. The central spring force is

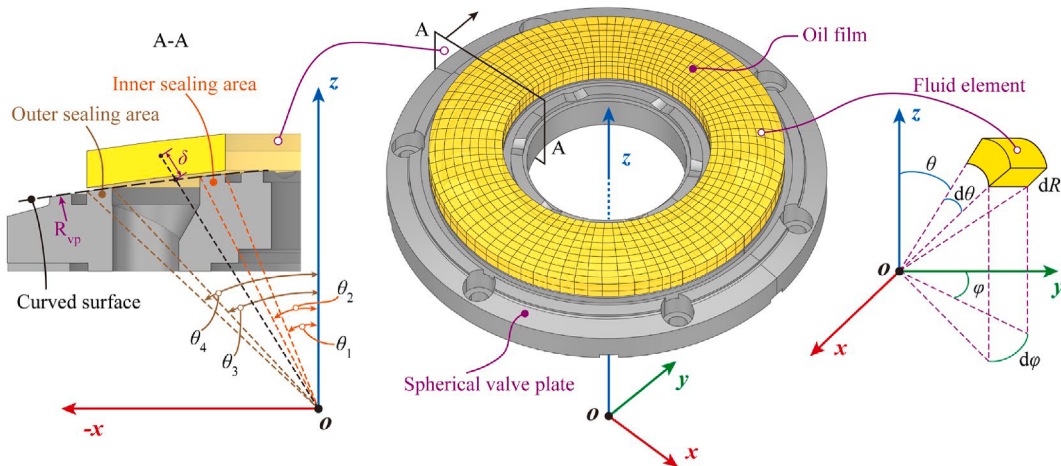


Fig. 5. Diagram of SVP's partial size and oil film meshing.

increased to maintain the oil film thickness at a suitable value. Therefore, the micron-level oil film thickness variation puts high demands on the selection of central spring force.

2.2. Fluid model

Eq. (21) and Eq. (22) indicate that the external forces and moments on the CCB need to be balanced by oil film reaction forces. Fig. 5 illustrates the oil film of SVPP. Notice that the micron-level oil film thickness is exaggerated for illustrative purposes. The fluid coordinate system (x , y , z) associated with the oil film is established, while the origin selects the circle center of the SVP curved surface. z and y -axis are parallel to Z and Y -axis respectively, and the x -axis is determined by the right-hand rule. In addition, a spherical coordinate system (R , θ , φ) equivalent to (x , y , z) is defined, by considering the shape of the oil film. Referring to the concept of longitude and latitude lines, θ and φ -direction is called longitude and latitude direction, respectively. Coordinate transformation equations are also given:

$$\begin{cases} x = R\sin\theta\sin\varphi \\ y = R\sin\theta\cos\varphi \\ z = R\cos\theta \end{cases} \quad (23)$$

As shown in Fig. 5, the oil film is meshes using spherical coordinate units (dR , $d\theta$, $d\varphi$). A fluid element is selected for force analysis. Before the analysis, the following assumptions are stated:

- (1) the oil is an ideal Newtonian fluid with constant density;
- (2) ignoring the effect of gravity;
- (3) no slippage of oil film near the wall surface;
- (4) hydraulic flow characteristics are laminar flow;
- (5) the pressure stays constant in the direction of oil film thickness.

Analyze the forces acting on fluid elements to generate equilibrium equations in the latitude direction:

$$\begin{aligned} pRdRd\theta + \left(\tau + \frac{\partial\tau}{\partial R} dR \right) R^2 \sin\theta d\theta d\varphi \\ = \left(p + \frac{\partial p}{\partial \varphi} d\varphi \right) RdRd\theta + \tau R^2 \sin\theta d\theta d\varphi \end{aligned} \quad (24)$$

Eq. (24) simplifies to:

$$\frac{\partial\tau}{\partial R} = \frac{1}{R\sin\theta} \frac{\partial p}{\partial \varphi} \quad (25)$$

With Newton's law of internal friction (Eq. (26)), Eq. (25) can be rearranged as:

$$\tau = \mu \frac{\partial v_\varphi}{\partial R} \quad (26)$$

$$\frac{\partial}{\partial R} (\mu \frac{\partial v_\varphi}{\partial R}) = \frac{1}{R\sin\theta} \frac{\partial p}{\partial \varphi} \quad (27)$$

As the $-xz$ plane shown in Fig. 5, a straight line is launched from the origin to any point inside the oil film, and the distance from this point to the curved surface is called δ . Considering that δ is in the micron range, a simplified equation is obtained:

$$R = R_{vp} + \delta \rightarrow R \approx R_{vp} \quad (28)$$

$$\frac{\partial}{\partial R} \frac{\partial}{\partial \delta}$$

Substituting Eq. (28) into Eq. (27) and integrating twice over the thickness, the expression for latitude velocity of the fluid element is obtained:

$$v_\varphi = \frac{\delta^2}{2\mu R_{vp}\sin\theta} \frac{\partial p}{\partial \varphi} + \frac{\delta}{\mu} C_1 + C_2 \quad (29)$$

Considering the boundary conditions (Eq. (30)) of latitude velocity. The latitude velocity of fluid element becomes:

$$\begin{cases} \delta = 0, v_\varphi = 0 \\ \delta = h, v_\varphi = v_{cy} = \omega R_{vp}\sin\theta \end{cases} \quad (30)$$

$$v_\varphi = \frac{(\delta^2 - h\delta)}{2\mu R_{vp}\sin\theta} \frac{\partial p}{\partial \varphi} + \frac{v_{cy}\delta}{h} \quad (31)$$

Similarly, the equations of fluid element longitude force balance and longitude velocity can be derived:

$$\begin{aligned} pR\sin\theta dRd\varphi + \left(\tau + \frac{\partial\tau}{\partial R} dR \right) R^2 \sin\theta d\theta d\varphi + \rho R^2 \sin\theta dRd\theta d\varphi \frac{v_\varphi^2}{R\sin\theta} \\ = \left(p + \frac{\partial p}{\partial \theta} d\theta \right) R\sin\theta dRd\varphi + \tau R^2 \sin\theta d\theta d\varphi \end{aligned} \quad (32)$$

$$\begin{aligned} v_\theta = \frac{\delta^2}{2\mu R_{vp}} \frac{\partial p}{\partial \theta} - \frac{\rho}{4\mu^3 R_{vp}^3 \sin^3\theta} \left(\frac{\delta^6}{30} - \frac{\delta^5 h}{10} + \frac{\delta^4 h^2}{12} \right) \left(\frac{\partial p}{\partial \varphi} \right)^2 \\ - \frac{\rho v_{cy}^2}{12h^2 \mu R_{vp} \sin\theta} \delta^4 - \frac{\rho v_{cy}}{\mu^2 R_{vp}^2 \sin^2\theta} \left(\frac{\delta^5}{20h} - \frac{\delta^4}{12} \right) \frac{\partial p}{\partial \varphi} + \frac{\delta}{\mu} C_3 + C_4 \end{aligned} \quad (33)$$

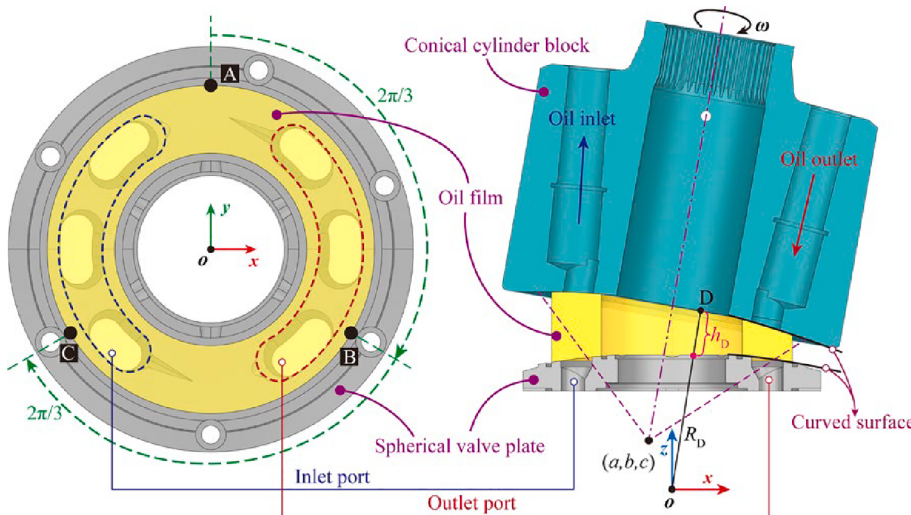


Fig. 6. Diagram of the oil film thickness of SVPP.

Eq. (33) combined with the longitude velocity boundary conditions (Eq. (34)) can be written as:

$$\begin{cases} \delta = 0, v_\theta = 0 \\ \delta = h, v_\theta = 0 \end{cases} \quad (34)$$

$$\begin{aligned} v_\theta &= \frac{\delta^2 - h\delta}{2\mu R_{vp}} \frac{\partial p}{\partial \theta} - \frac{\rho}{4\mu^3 R_{vp}^3 \sin^3 \theta} \left(\frac{\delta^6}{30} - \frac{h\delta^5}{10} + \frac{h^2\delta^4}{12} - \frac{h^5\delta}{60} \right) \left(\frac{\partial p}{\partial \varphi} \right)^2 \\ &\quad + \frac{\rho v_{cy}^2}{12\mu R_{vp} \sin \theta} \left(h\delta - \frac{\delta^4}{h^2} \right) - \frac{\rho v_{cy}}{\mu^2 R_{vp}^2 \sin^2 \theta} \left(\frac{\delta^5}{20h} - \frac{\delta^4}{12} + \frac{h^3\delta}{30} \right) \frac{\partial p}{\partial \varphi} \end{aligned} \quad (35)$$

Neglecting the higher-order items in it:

$$v_\theta = \frac{\delta^2 - h\delta}{2\mu R_{vp}} \frac{\partial p}{\partial \theta} + \frac{\rho v_{cy}^2}{12\mu R_{vp} \sin \theta} \left(h\delta - \frac{\delta^4}{h^2} \right) \quad (36)$$

The flow continuity equation for an incompressible fluid in spherical coordinates is:

$$\frac{\partial v_\delta}{\partial \delta} + \frac{2v_\delta}{R_{vp}} + \frac{1}{R_{vp}} \frac{\partial v_\theta}{\partial \theta} + \frac{v_\theta \cot \theta}{R_{vp}} + \frac{1}{R_{vp} \sin \theta} \frac{\partial v_\varphi}{\partial \varphi} = 0 \quad (37)$$

Substituting Eqs. (31) and (36) into Eq. (37), and integrating along the direction of thickness yields the Reynolds equation for SVPP:

$$\begin{aligned} &\frac{1}{\mu R_{vp}^2} \frac{\partial}{\partial \theta} \left(h^3 \frac{\partial p}{\partial \theta} \right) + \frac{h^3 \cot \theta}{\mu R_{vp}^2} \frac{\partial p}{\partial \theta} + \frac{1}{\mu R_{vp}^2 \sin^2 \theta} \frac{\partial}{\partial \varphi} \left(h^3 \frac{\partial p}{\partial \varphi} \right) \\ &= \frac{3\rho}{10\mu R_{vp}^2} \frac{\partial}{\partial \theta} \left(\frac{v_{cy}^2 h^3}{\sin \theta} \right) + \frac{3\rho v_{cy}^2 h^3 \cot \theta}{10\mu R_{vp}^2 \sin \theta} + \frac{6}{R_{vp} \sin \theta} \frac{\partial}{\partial \varphi} (v_{cy} h) + 12 \frac{\partial h}{\partial t} \end{aligned} \quad (38)$$

According to Eq. (38), the distribution of oil film thickness and its rate of change are necessary to find the value of pressure. Therefore, the next step is to solve the oil film thickness. Fig. 6 illustrates the method to calculate oil film thickness.

As shown in Fig. 6, there are three measurement points (A, B, C) with various locations installed in SVP. A line is launched from the origin through A, B, and C respectively, and the corresponding (A', B', C') is produced at the bottom of CCB. It was possible to set up the entire oil film thickness distribution by capturing the oil film thickness at three separate locations. The coordinates of points for the SVPP are:

$$\begin{aligned} \begin{bmatrix} A \\ B \\ C \end{bmatrix} &= \begin{bmatrix} R_{vp} & \theta_4 & 0 \\ R_{vp} & \theta_4 & 2\pi/3 \\ R_{vp} & \theta_4 & 4\pi/3 \end{bmatrix} \begin{bmatrix} A' \\ B' \\ C' \end{bmatrix} \\ &= \begin{bmatrix} R_{cyA} & \theta_4 & 0 \\ R_{cyB} & \theta_4 & 2\pi/3 \\ R_{cyC} & \theta_4 & 4\pi/3 \end{bmatrix} \begin{cases} R_{cyA} = R_{vp} + \delta_A \\ R_{cyB} = R_{vp} + \delta_B \\ R_{cyC} = R_{vp} + \delta_C \end{cases} \end{aligned} \quad (39)$$

Bring the right-angle coordinates of three measured points on the CCB into the spherical equation:

$$\begin{cases} (0-a)^2 + (R_{cyA} \sin \theta_4 - b)^2 + (R_{cyA} \cos \theta_4 - c)^2 = R_{vp}^2 \\ \left(\frac{\sqrt{3}}{2} R_{cyB} \sin \theta_4 - a\right)^2 + \left(-\frac{1}{2} R_{cyB} \sin \theta_4 - b\right)^2 + (R_{cyB} \cos \theta_4 - c)^2 = R_{vp}^2 \\ \left(-\frac{\sqrt{3}}{2} R_{cyC} \sin \theta_4 - a\right)^2 + \left(-\frac{1}{2} R_{cyC} \sin \theta_4 - b\right)^2 + (R_{cyC} \cos \theta_4 - c)^2 = R_{vp}^2 \end{cases} \quad (40)$$

The spherical center coordinates (a, b, c) and the spherical equation of the CCB bottom surface can be derived by Eq. (40). Further, for any point (D) on the SVPP oil film, h can be found with known θ_{cyD} and φ_{cyD} .

$$\begin{aligned} &(R_{cyD} \sin \theta_{cyD} \sin \varphi_{cyD} - a)^2 + (R_{cyD} \sin \theta_{cyD} \cos \varphi_{cyD} - b)^2 \\ &\quad + (R_{cyD} \cos \theta_{cyD} - c)^2 = R_{vp}^2 \end{aligned} \quad (41)$$

To obtain the thickness variation rate of D, the following equation are considered:

$$\begin{aligned} &2R_{cyD} \frac{\partial R_{cyD}}{\partial t} + 2a \frac{\partial a}{\partial t} + 2b \frac{\partial b}{\partial t} + 2c \frac{\partial c}{\partial t} \\ &- 2 \frac{\partial R_{cyD}}{\partial t} (a \sin \theta_{cyD} \sin \varphi_{cyD} + b \sin \theta_{cyD} \cos \varphi_{cyD} + c \cos \theta_{cyD}) \\ &- 2R_{cyD} (\sin \theta_{cyD} \sin \varphi_{cyD} \frac{\partial a}{\partial t} + \sin \theta_{cyD} \cos \varphi_{cyD} \frac{\partial b}{\partial t} + \cos \theta_{cyD} \frac{\partial c}{\partial t}) \\ &= 0 \end{aligned} \quad (42)$$

There are four unknown terms in Eq. (42), and a closed system of equations can be formed by differentiating Eq. (40), combined with a zero initial rate of thickness variation, the result can be deduced.

2.3. Leakage calculation

As shown in Fig. 7, there are three flow directions of SVPP leakage: q_{outer} flow over the outer sealing area, q_{inner} flow over the inner sealing area, and q_{window} flow from the high-pressure window to the low-

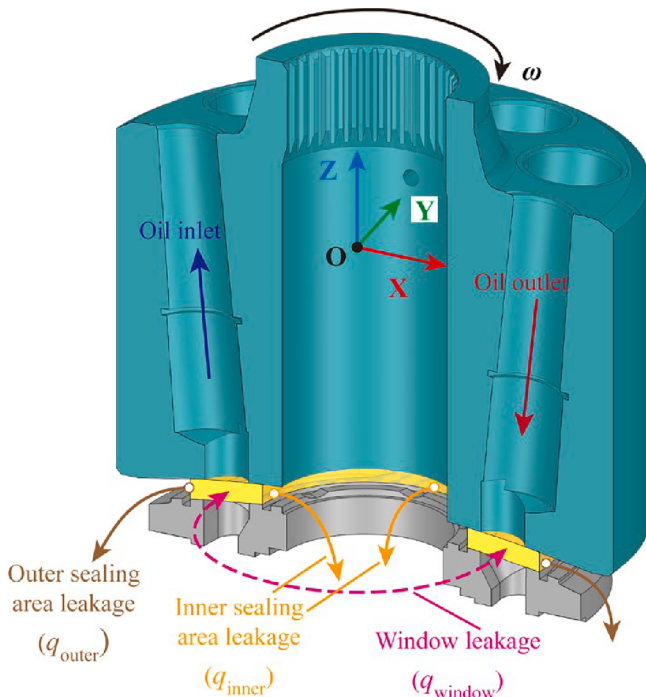


Fig. 7. Diagram of leakage of SVPP.

pressure window. q_{outer} and q_{inner} flow enters the case and eventually discharge via pump's drain port, and these flow losses result in a decrease in volumetric efficiency. The flow from the q_{window} re-enters the pump's working cycle and does not affect the volumetric efficiency [46,47].

The exact model for calculating SVPP leakage is derived from the established oil film lubrication model. For example, the q_{inner} is the leakage of all fluid elements at the inner boundary, which can be gained by calculating the longitude velocity and flow area of a fluid element. It should be noted in the calculation that the oil film thickness is not uniform and causes the fluid element number on the inner boundary to be different for different angles. Therefore, the q_{inner} is calculated as:

$$q_{\text{inner}} = \sum_{j=1}^{2\pi/d\varphi} \sum_{i=1}^{h_{r1}(\varphi)/d\delta} (v_\theta)_{ij} r_1 d\theta d\delta \quad (43)$$

Similarly, the leakage at the outer boundary and the total leakage are given by:

$$q_{\text{leakage}} = q_{\text{inner}} + q_{\text{outer}} = \sum_{j=1}^{2\pi/d\varphi} \sum_{i=1}^{h_{r1}(\varphi)/d\delta} (v_\theta)_{ij} r_1 d\theta d\delta + \sum_{j=1}^{2\pi/d\varphi} \sum_{k=1}^{h_{r4}(\varphi)/d\delta} (v_\theta)_{kj} r_4 d\theta d\delta \quad (44)$$

3. Numerical solution

In this study, the Reynolds equation is discretized by FVM, and the method was derived in detail in [2,16,48]. It will not be repeated in this paper. After meshing the oil film by the method in Section 2.2, the parameter information for each fluid element (i.e., the control volume in FVM) is concentrated at the element's nodes. Furthermore, as assumption five in Section 2.2, the oil film pressure field is discretized into a 2D matrix, and the annular feature of the oil film makes the matrix feasible for the circular iterative solution. Combined with the pressure boundary conditions, the circular tridiagonal matrix algorithm is used to solve for the pressure on the same annular oil film, and the entire oil film pressure can then be obtained by sequentially expanding the annulus. The pressure iteration error is shown below:

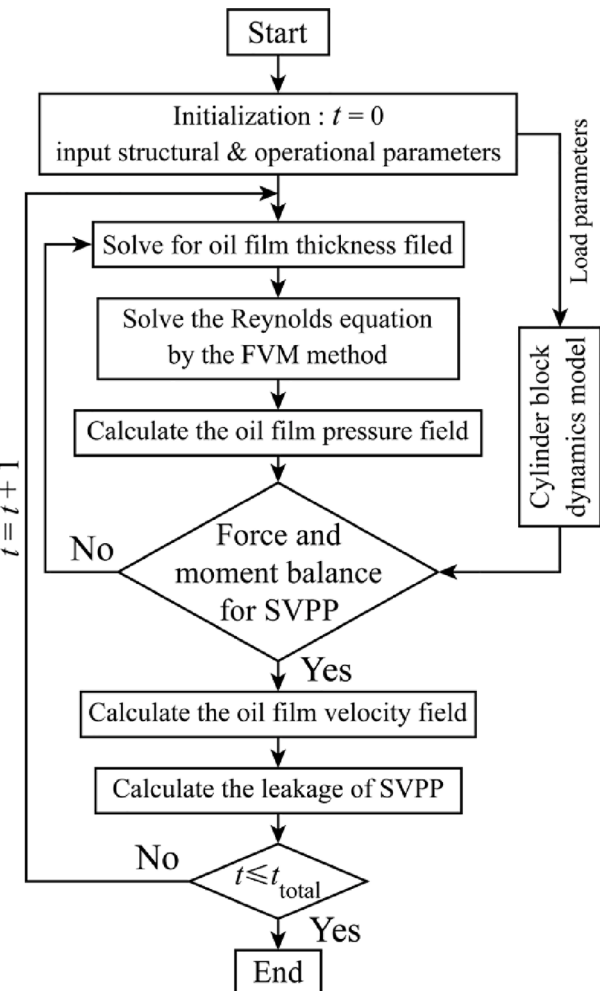


Fig. 8. Flow chart of the leakage calculation model.

Table 1
Part of simulation parameters.

No.	Parameters	Details
1	number of pistons	9
2	pump displacement	750 mL/r
3	inclined angle of piston	5°
4	inclined angle of swashplate	15°
5	radius of spherical valve plate curved surface	590 mm
6	angle of inside edge of inner sealing area	5.2°
7	angle of outside edge of inner sealing area	5.9°
8	angle of inside edge of outer sealing area	8.2°
9	angle of outside edge of outer sealing area	8.9°
10	diameter of piston	45 mm
11	mass of piston and slipper	1.74 kg
12	inlet pressure	0.1 MPa
13	hydraulic oil type	L-HM 46
14	hydraulic oil kinematic viscosity (under 40 °C)	46 mm ² /s
15	density of hydraulic oil	875 kg/m ³
16	oil temperature	40 °C
17	model simulation time	5 rotations
18	pressure iteration error	0.1 Pa
19	fluid element size (dR × dθ × dφ)	0.5 mm × 0.5° × 0.5°

$$\left| \frac{p_{t+1} - p_t}{p_t} \right|_{\max} \leq \epsilon \quad (45)$$

When the pressures all satisfied Eq. (45), the oil film pressure field at the current time was obtained. Based on Eqs. (21) and (22), the cylinder block load should remain in equilibrium. Noting that the uncertainty in

Table 2
Working condition sets and groups.

Rotation speed (rpm)	Load pressure (MPa)	Group
500	10	W1
	15	W2
	20	W3
1000	10	W4
	15	W5
	20	W6

Eqs. (21) and (22) are the thickness, the Newton-Raphson algorithm is used to solve this non-linear system of equations iteratively until the thickness and pressure at the current moment make the equations valid. The oil film thickness and pressure at the current moment are brought into Eqs. (31) and (36) solve for the velocity field and the leak is finally obtained from Eq. (44).

Fig. 8 shows a flow chart of the numerical calculation model to solve for the SVPP leakage, the exact process is implemented in MATLAB. The structural and operational parameters of the pump need to be defined before simulation as shown in Tables 1 and 2. The pump operating parameters mainly comprise rotation speed and load pressure. It should be

noted that the parameters in Table 2 are based on the actual operation of the 750 mL/r pump in the TBM. There are two options for speed and three options for pressure.

3.1. Numerical result for leakage model

Fig. 9(a) shows the simulation results of the oil film thickness for six working conditions. φ_{azi} indicates the azimuth of the CCB tilt in the xy plane, and λ_{tilt} indicates the angle of the CCB tilt compared to the xy plane. Fig. 9(b) shows some oil film thickness data for six conditions, including minimum oil film thickness, maximum oil film thickness, and average oil film thickness for a certain condition.

As shown in Fig. 9(a), the color change is more pronounced at 1000 rpm than 500 rpm at the same load pressure. It means the increase in speed makes the oil film thickness fluctuate more, which is consistent with the variation λ_{tilt} . Such a variation is also reflected in the data of Fig. 9(b). This result contradicts the usual idea that an increase in speed improves the fluid dynamics, enabling an increase in oil film thickness and a smaller fluctuation range. The explanation for this phenomenon is that the increase in speed also increases radial inertia force on the piston-slipper assembly, which consequently causes the CCB to tilt more.

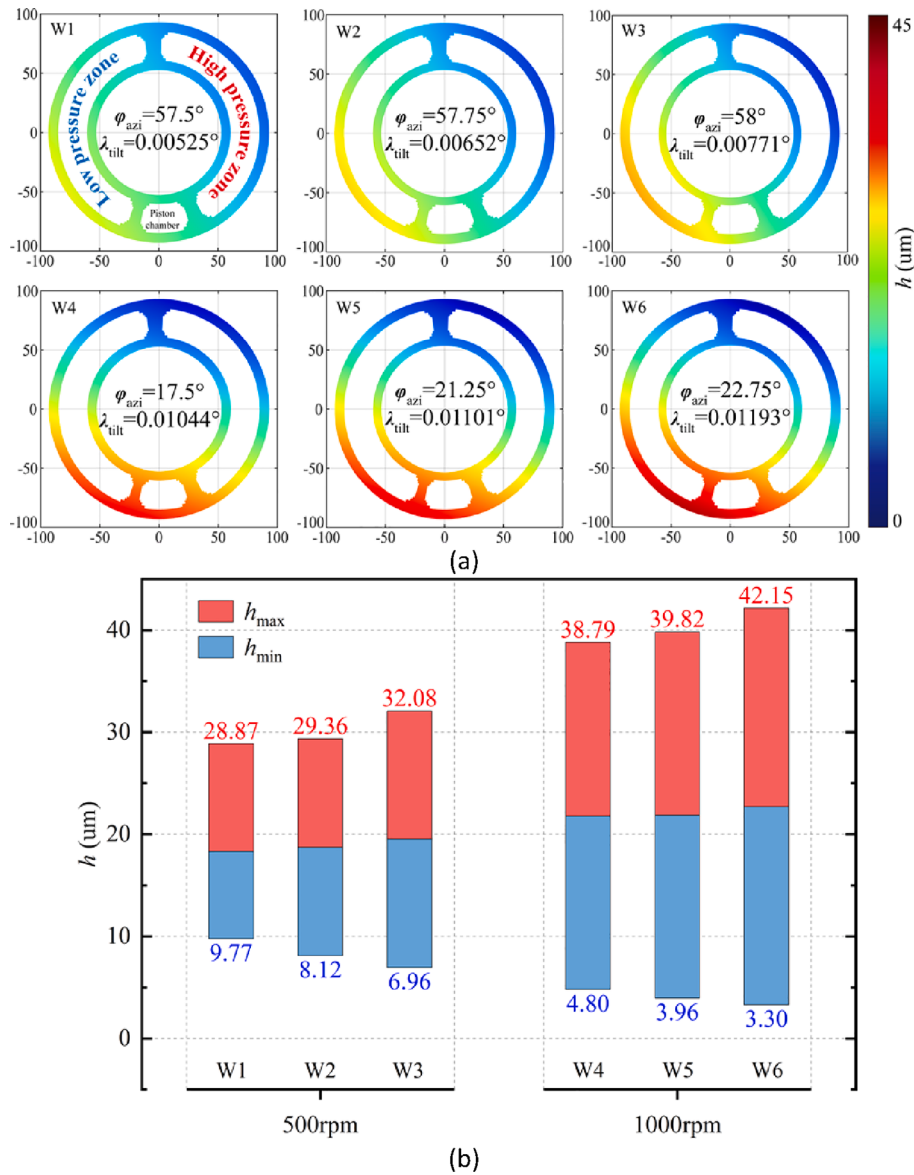


Fig. 9. (a) Diagram of oil film thickness distribution; (b) Oil film thickness simulation data.

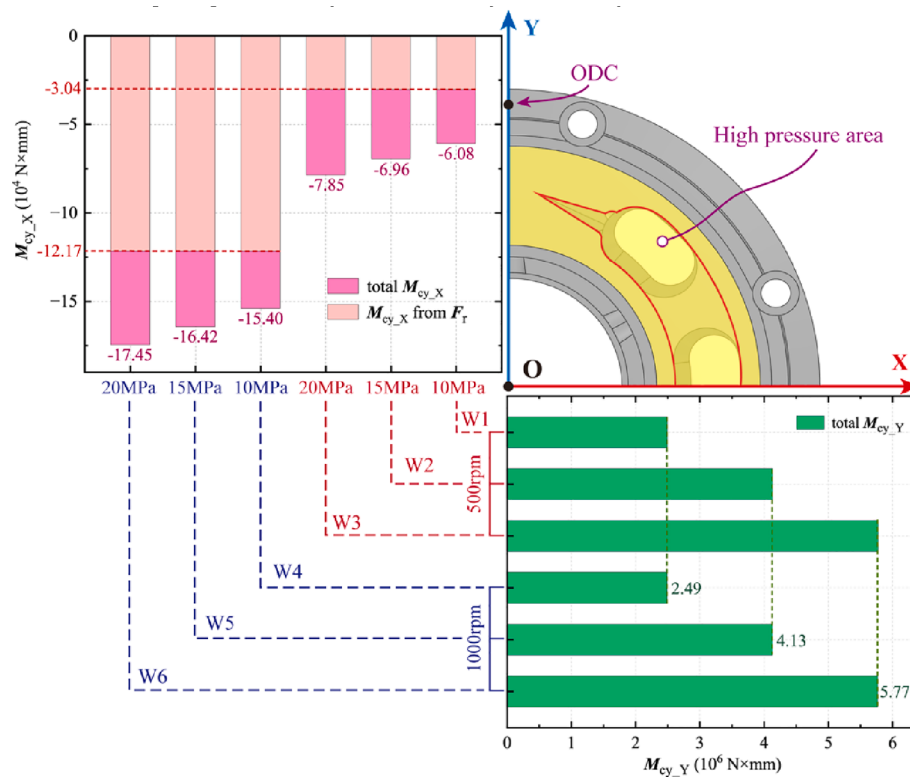


Fig. 10. Tilt moment of CCB under different working conditions.

According to Section 2.1, the tilt behavior of CCB depends on the moment around the X-axis and Y-axis. By Eq. (22), the X-axis moment is mainly caused by piston chamber pressure, swashplate support reaction force, and radial inertia force; the Y-axis torque is mainly caused by piston chamber pressure. The CCB tilt moment data for six working conditions are shown in Fig. 10. Higher speed increases the torque of M_{cy_X} , while M_{cy_Y} does not change significantly, since it depends on pressure.

According to Fig. 10, M_{cy_X} and M_{cy_Y} tilt the CCB toward ODC and high-pressure area, respectively. There are two effects of increasing rotation speed: first, the hydrodynamic force is improved so that the oil film carrying capacity increases, and the thickness increases overall; second, the trend of CCB tilt toward ODC increases, causing the oil film thickness to fluctuate more. The combined effect of tilt moment results makes CCB tilt toward ODC with increasing speed at the same pressure and tilts toward the high-pressure area with increasing pressure at the same speed. These phenomena and laws have been found in the literatures [31,49].

Leakage calculation of SVPP also requires the longitude velocity of the fluid. Considering Eq. (34), the longitude velocity field is divided into nine layers along the thickness direction, and the layer with the largest value (layer five) is selected as the demonstration, as shown in Fig. 11(a). Fig. 11(b) shows the data of the speed layer, “-” and “+” means oil flows toward the center and pump case, respectively.

Based on Eq. (36), it can be found that the longitude velocity contains differential pressure action term and centrifugal action term, with the former playing the major role. Comparing the simulation results of Fig. 10, the increases in load pressure and rotation speed both lead to an increase in longitude velocity. Moreover, the velocity in the outer area is always greater than that in the inner area, regardless of the working conditions.

Another phenomenon in Fig. 11(a) is that the larger velocity values are concentrated at 5 o'clock, which has two reasons behind this. First, at the current time of simulation, a piston has just moved into the transition zone near IDC, as shown in Fig. 9(a). Compared to the ODC, the

above zone generates a greater differential pressure effect due to the pressurized oil in the piston chamber. The other reason is that the tilt of CCB results in a larger thickness of oil film near IDC, which makes oil flow easier in the longitude direction under the same centrifugal action.

Fig. 12(a) shows the leakage of SVPP, which was calculated using the thickness and longitude velocity data. With leakage data, the effect of pressure and speed on leakage can be yielded, and the specific analysis is given below.

The 10 MPa leakage at two speeds was selected separately as the benchmark, and the data in Fig. 12(a) were dimensionless processed. The obtained ratio is shown as the red line in Fig. 12(b). It can be found that as the pressure increases, the growth of leakage at 500 rpm is gradually greater than that at 1000 rpm. For the oil film thickness, it means unbalanced pressure is the dominant factor of CCB tilt at low speed and high pressure conditions. The performance is CCB tilt azimuth closer to the middle of the high-pressure area and can be verified from the Fig. 9. For the velocity field, it means the gain of differential pressure effect on the longitude velocity at low speed is greater than the effect at high speed. Therefore, the pump should avoid operation at low speeds and high pressure conditions to prevent excessive leakage.

Three leakages at 500 rpm were chosen as the benchmark, and the leakages at 1000 rpm were dimensionless processed respectively. The obtained ratios are shown as blue lines in Fig. 12(b). It can be found that the overall change in the contribution of both speed variations to the leakage growth at different pressures is small and slightly decreasing. The leakage ratio of two speeds at 10 MPa is used as an example to analyze the cause.

According to Eqs. (22) and (36), the fixed load pressure keeps the Y-axis moment of CCB and the differential pressure term of fluid longitude velocity constant. The increased rotation speed enhances the radial inertia force and the centrifugal action term in fluid longitude velocity, making a greater tendency of the CCB around the x-axis and greater leakage. But the inertia overturning moment caused by rotation speed is smaller than the hydraulic overturning moment caused by pressure. This ratio decreases with increasing pressure, which leads to a decrease in the

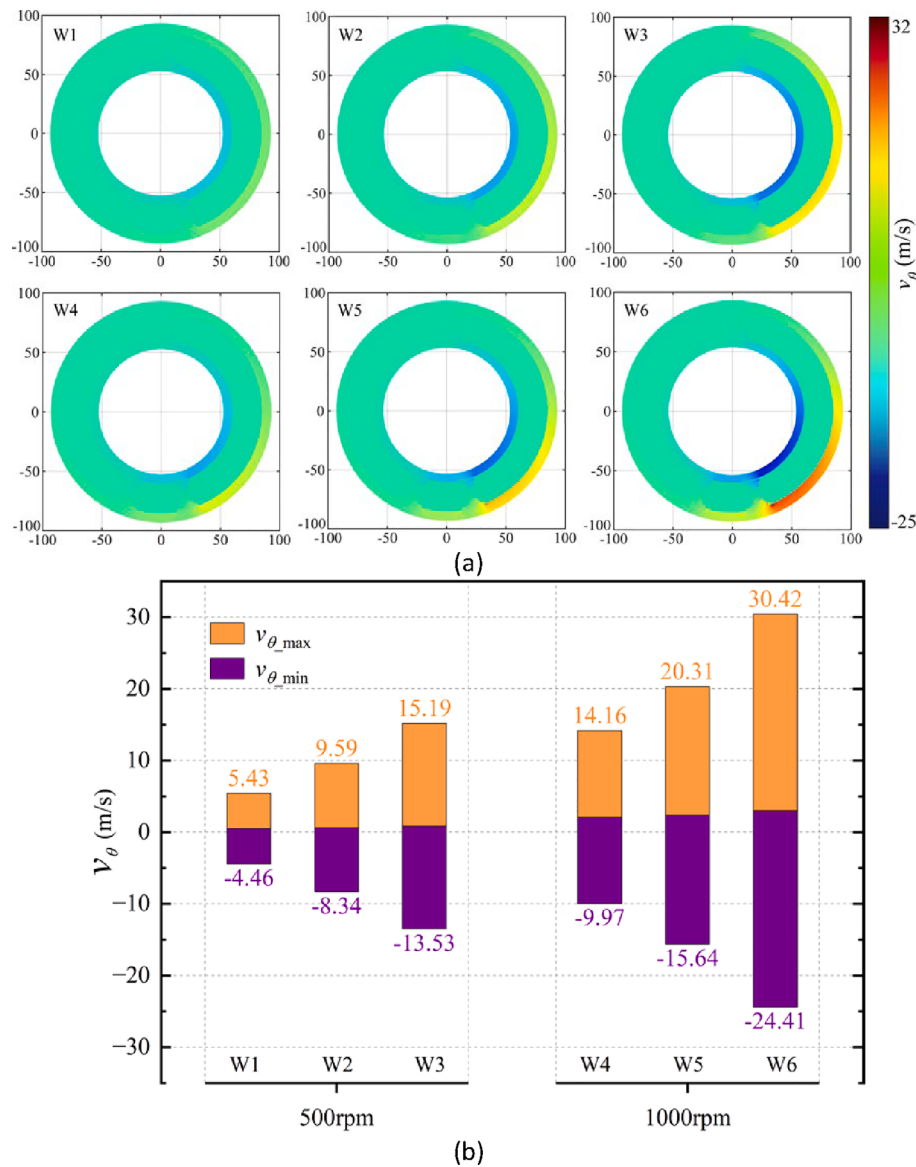


Fig. 11. (a) Diagram of oil film longitude velocity distribution (layer five); (b) Oil film longitude velocity simulation data (layer five).

effect of rotation speed on CCB tilt at high pressure, so the blue line in Fig. 12(b) shows a decreasing trend.

3.2. Parametric analysis of spring stiffness

In this section, the effect of central spring stiffness on leakage is analyzed. According to Section 2.1, the spring preload becomes part of the swashplate support reaction force through the swashplate conversion. The rotation speed affects the swashplate support reaction force via radial inertia force, which disturbs the effect of spring. Therefore, 1000 rpm is selected as the fixed speed to highlight the effect of spring stiffness on the leakage. The simulation conditions are shown in Table 3, in which the spring stiffness is selected from the actual pump and set with a $\pm 5\%$ tolerance.

Fig. 13 shows the oil film thickness for different spring stiffnesses, and the variation of it still follows the rule in Section 3.1 under a given spring stiffness. Comparing the oil film thickness fields for different spring stiffnesses at the same pressure, it can be found that the fluctuation range and the average value of thickness show a decreasing trend as the spring stiffness increases.

Fig. 13 shows that the average thickness decreases with increasing

spring stiffness. According to Eq. (21), the balance of piston chamber pressure, spring force, and oil film carrying force determines an initial oil film thickness. CCB squeezes the oil film under the action of tilt moment, which leads to a fluctuation of thickness. At constant load pressure, the greater the spring force, the more the oil film is squeezed.

Fig. 14 displays the specifics of CCB tilt moments for different spring stiffnesses. The tilt and azimuth angles under the same spring stiffness still follow the previous rules, i.e., an increase in pressure causes the tilt increase and CCB to be towards the high-pressure area. As the spring stiffness increases at the same pressure, the tilt azimuth is closer to ODC and the CCB tilt is improved.

An interesting phenomenon was found when comparing Figs. 9 and 14. The increase in speed and spring stiffness makes the CCB tilt azimuth close to ODC, but the variation of the CCB tilt angle is diametrically opposite. Reasons for the above tilt behavior were specifically analyzed in conjunction with CCB dynamics.

For the CCB tilt azimuth: First, the load pressure dominates the moment $M_{cy,Y}$ of CCB, which is independent of speed and spring stiffness. Second, the increase in spring stiffness and speed induces improvement in the swashplate reaction force and radial inertia force. These tilt CCB toward ODC.

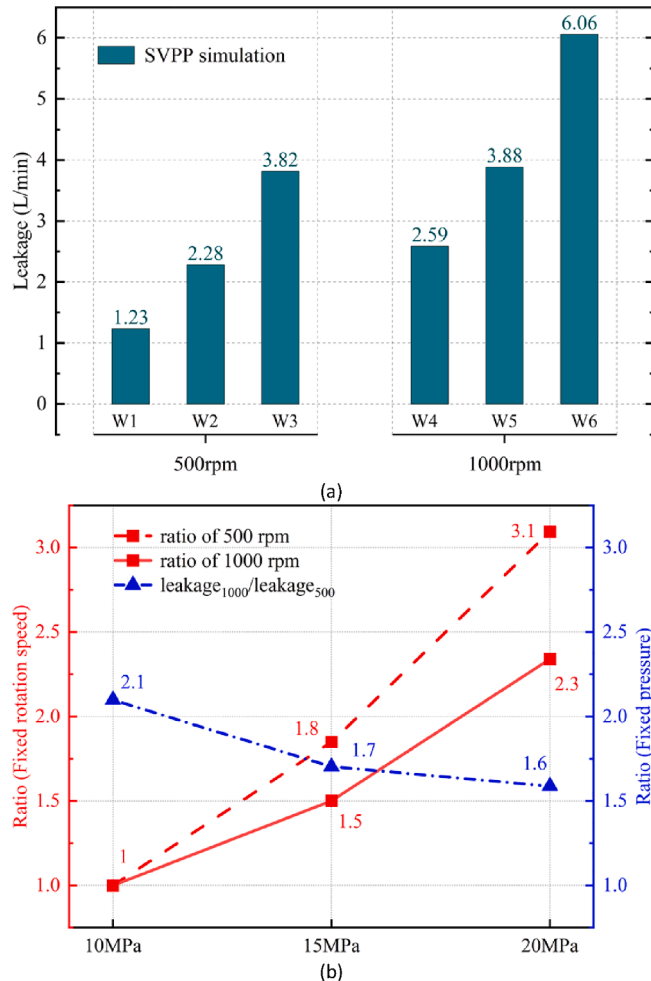


Fig. 12. (a) Leakage simulation results of SVPP in six working conditions; (b) Diagram of leakage ratio variation.

Table 3
Condition sets and groups for different spring stiffnesses.

Spring stiffness (N/mm)	Load pressure (MPa)	Group
209	10	S1
	15	S2
	20	S3
220	10	S4
	15	S5
	20	S6
231	10	S7
	15	S8
	20	S9

For the CCB tilt angle: First, the hydrodynamic enhancement from speed growth fails to offset the deterioration in tilt [49]. Second, the increased spring force compresses the oil film, which enhances the dynamic and squeeze effects in Eq. (38). This creates a “load equalization” effect where the oil film resists CCB tilt more possibly. As a result, two opposite results are formed in Fig. 9, and Fig. 14.

Fig. 15 shows the longitude velocity field, and the data still come from layer five. According to Eq. (36), the change in spring stiffness has no significant effect on the longitude velocity, so the difference in velocity in Fig. 11 is due to the different load pressure and oil film thickness for each working condition. In brief, the rise of load pressure enhances the longitude velocity, and the rise of spring stiffness reduces the overall thickness and fluctuation of oil film, resulting in a better

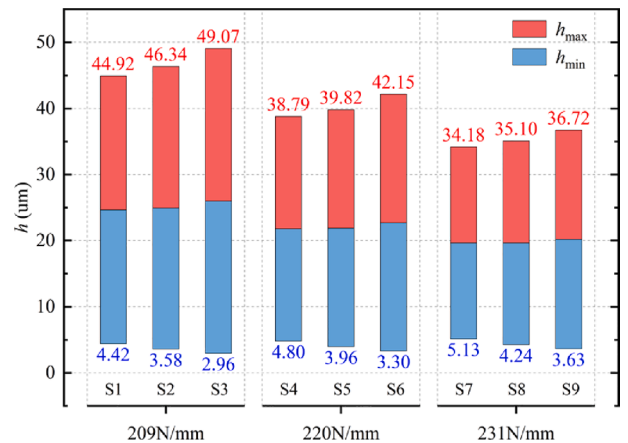


Fig. 13. Oil film thickness under different spring stiffness.

sealing effect and less longitudinal flow of oil.

Fig. 16 shows the SVPP leakage for different stiffness. Under the same pressure, the higher the spring stiffness, the smaller the corresponding leakage. Because both the oil film thickness and longitude velocity, which determine the leakage, decrease as the spring stiffness increases, as shown in Fig. 13 and Fig. 15.

Fig. 16 shows the leakage ratio indicated by the dashed segment. Ratios are calculated by taking the 220 N/mm leakage as a standard and dividing the leakage of remaining spring stiffness by it, and they are further distinguished by pressure. The ratio of 231/ 220 is less than 1 and remains stable, which indicates that the appropriate increase in spring stiffness to reduce leakage applies to different pressure ranges. The ratio of 209/ 220 is greater than 1 and tends to decrease because the increased pressure suppresses the leak growth caused by the stiffness drop. Comparing the red and blue lines, the leakage gap caused by the ± 5% stiffness tolerance is 237%.

4. Experiment

This section tested the total leakage of the 750 mL/r pump with a test bench, aiming to verify the validity of the developed leakage model. Specifically, the test was set up for two pumps with different spring stiffnesses, pump A (209 N/mm) and pump B (220 N/mm). The operating conditions are shown in Table 3 (S1 ~ S6), and the pump rotation speed is fixed at 1000 rpm. Some parameters of the test bench are shown in Table 4.

Fig. 17 shows the pump test bench and its principle. The test bench mainly consists of a drive section, a test pump, a loading section, and a control & data recording system. Specifically, the drive part uses multiple motors to power the loading pump output pressurized oil, which is fed to the drive motor and eventually turns the test pump; the loading part uses a proportional pressure relief valve to control the outlet pressure of the test pump; the control & data recording system monitors and records leakage of the test pump. A brief description of the experimental process is as follows: The swashplate tilt angle is adjusted and fixed at a certain angle before the experiment begins; the speed and pressure are adjusted to reach the specified working conditions; after the pump runs for a period and achieves a stable state, the leakage data is recorded. In particular, the inlet oil temperature of the pump should be maintained at 25 ~ 40°C to reduce the effect of temperature. Finally, the experiments were repeated several times to ensure the reliability of the data.

1-Loading pump; 2- Coupling; 3-Motor; 4-Safety valve; 5-One way valve; 6-Directional valve; 7- Drive motor; 8- Pressure sensor; 9- Speed and torque sensor; 10—750 mL/r axial piston pump; 11- Proportional pressure relief valve; 12- Flowmeter; 13- Temperature Sensor; 14- Oil tank.

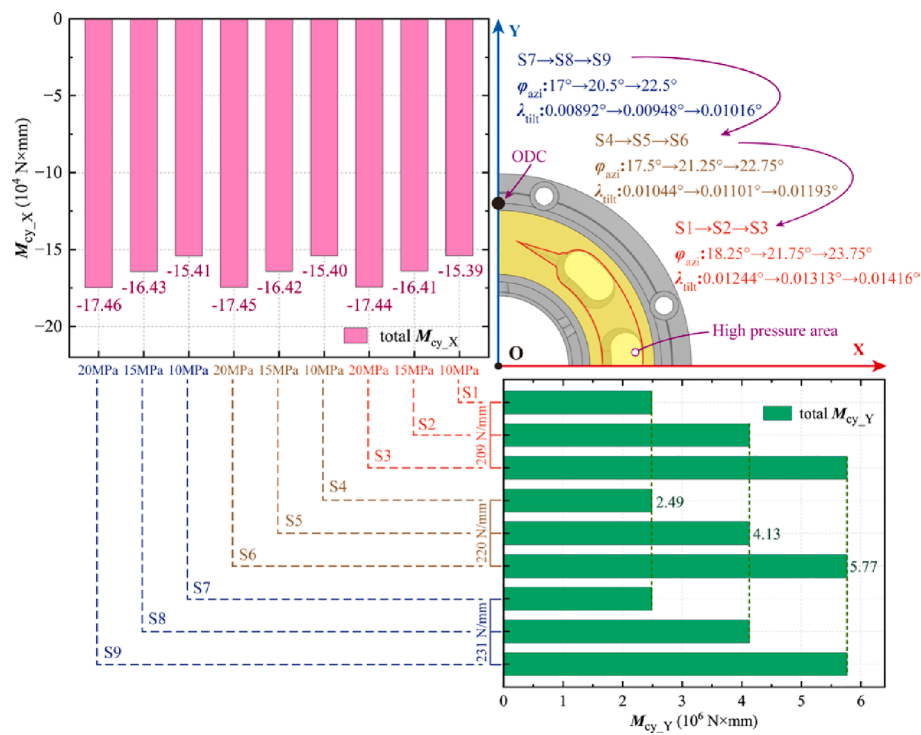


Fig. 14. Tilt moment of CCB under different spring stiffness.

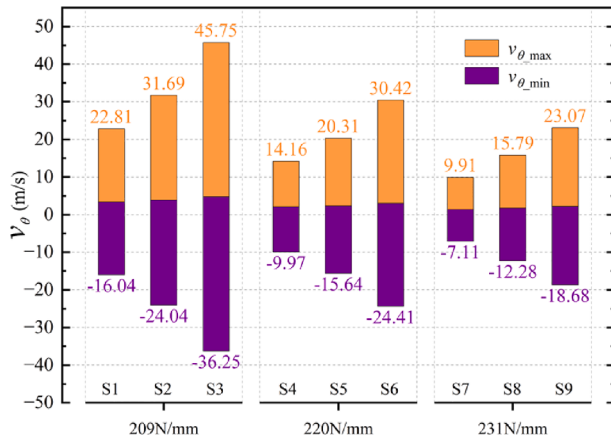


Fig. 15. Oil film longitude velocity under different stiffness.

Fig. 18 shows the experimental results of pump total leakage and the SVPP simulation results. The analysis of SVPP leakage can be found in Section 3.2. It can be seen that the total leakage, the SVPP leakage, and the percentage are significantly higher in pump A than those in pump B under the corresponding working conditions. The experimental results were compared and processed to obtain the independent effects of spring stiffness and pressure on the total leakage, as shown in Fig. 19.

From the left Y-axis of Fig. 19, it can be seen that the pump A to pump B leakage ratio is greater than 1 at each fixed pressure, as the reduced spring stiffness decreases the CCB's squeeze on the oil film. It is also noticeable that this ratio decreases with increasing pressure since the piston chamber pressure also has a squeezing effect on the CCB, which counteracts the negative effect of the reduced spring stiffness. The right Y-axis shows how the respective leakage of pump A and pump B increases as a multiple with increasing pressure. It can be seen that the increased pressure raises the leakage in both pumps, but the gain in pump A is smaller. As mentioned above, it is because the increase in pressure and the decrease in spring stiffness can weaken each other's

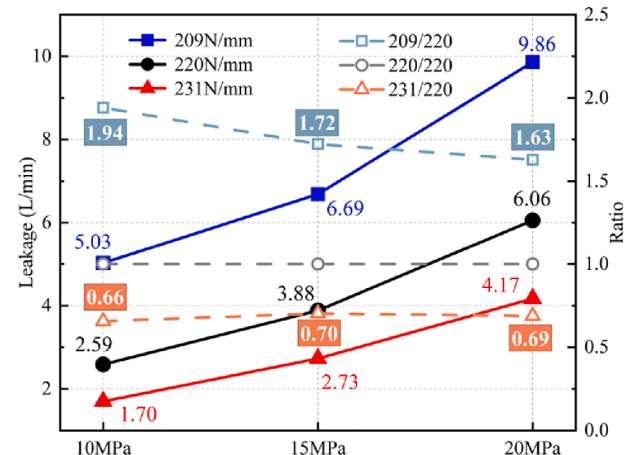


Fig. 16. Leakage simulation results and leakage ratio under different stiffness.

Table 4
Some sensor parameters of the test bench.

No.	Parameters	Details
1	measuring range of pressure sensor	0 ~ 40 MPa
2	temperature range of pressure sensor	-40~+125 °C
3	output signal of pressure sensor	4 ~ 20 mA
4	linearity of pressure sensor	<±0.25%
5	accuracy of pressure sensor	<±0.5% FS
6	measuring range of temperature sensor	-25~+100 °C
7	output signal of temperature sensor	4 ~ 20 mA
8	accuracy of temperature sensor	<±0.4% FS
9	measuring range of flowmeter	2 ~ 600 L/min
10	linearity of flowmeter	<±0.1%
11	accuracy of flowmeter	<±0.3%
12	maximum pressure rating of proportional pressure relief valve	42 MPa
13	Response sensitivity of proportional pressure relief valve	< 0.5%

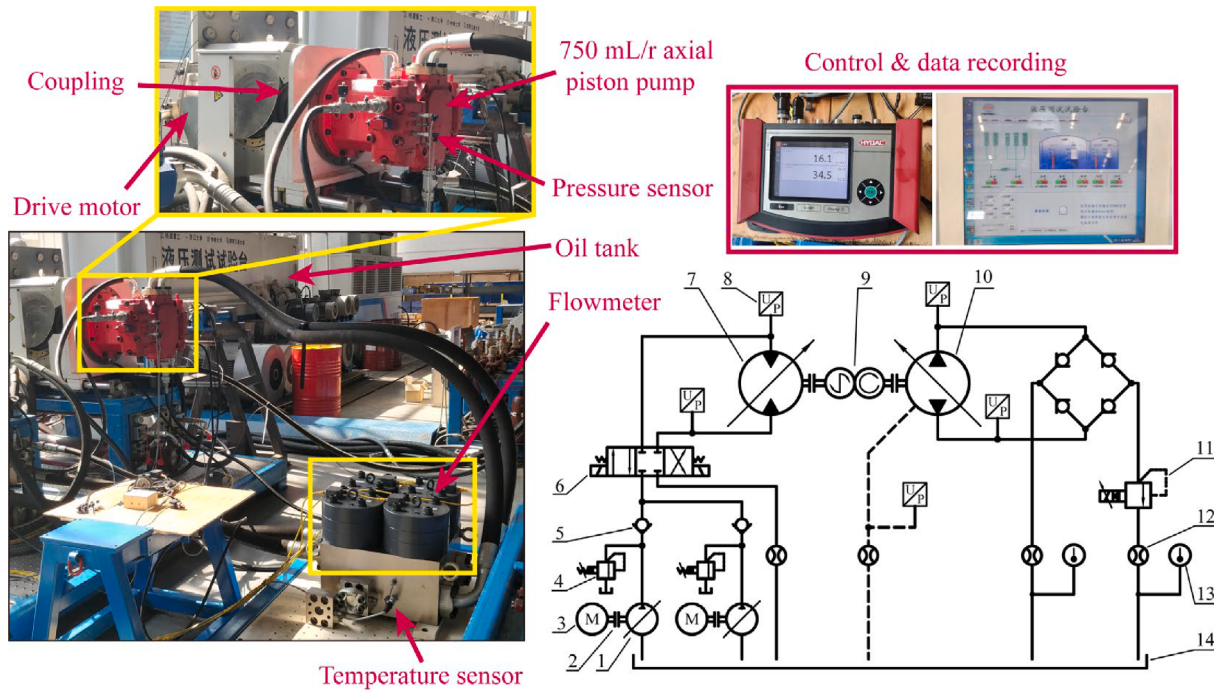


Fig. 17. Diagram of the leakage test bench.

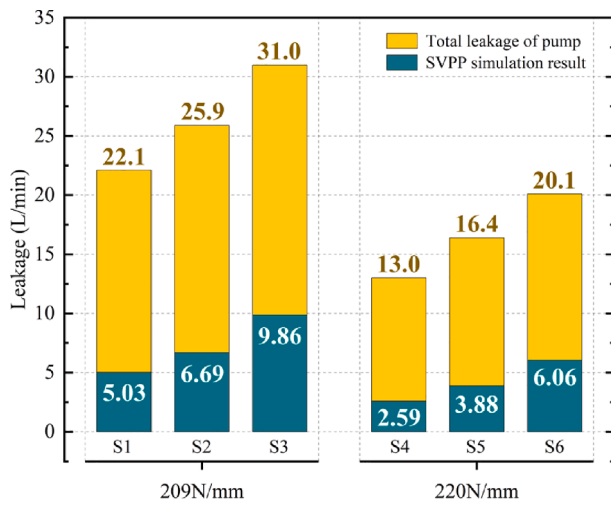


Fig. 18. Leakage data of 750 mL/r pump.

effect. Combining these ratios, pump A leaks 1.7 times more than pump B at low pressures, thus the pump with reduced spring stiffness should be avoided operating at low pressures.

The total leakage of 750 mL/r pumps is mainly generated by the three major friction pairs [50]. As the piston pair oil film generally has the thinnest thickness [2,51], the leakage from it is the smallest proportion to the total leakage and can be ignored [47].

The effect of spring stiffness on leakage is analyzed. Fig. 18 was processed to obtain the total leakage gap (ΔQ_{sp}) and SVPP leakage gap (Δq_{sp}) between pump A and pump B for the same working conditions, as well as the leakage gap ratio of SVPP gap to slipper pair leakage gap (ratio_{sp}), as shown in Table 5.

The SVPP and the slipper pair, both of which generate oil film by the same mechanism and are dominated by hydrostatic support, where leakage depends mainly on pressure and oil film thickness [52–54]. In qualitative analysis, as the two support ends of the rotating assembly in

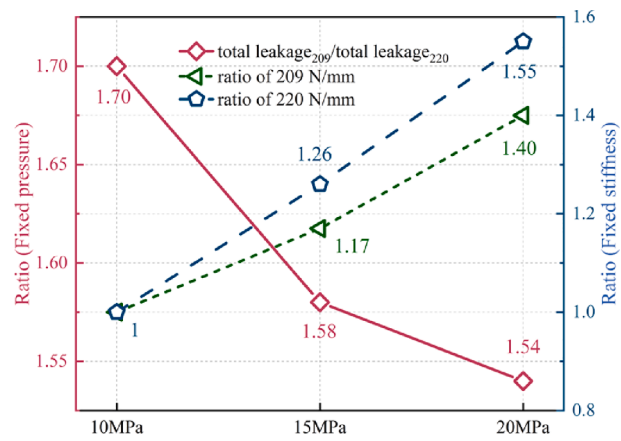


Fig. 19. Total leakage ratio of 750 mL/r pump.

Table 5
Comparison of leakage at different stiffnesses.

	Δq_{sp} (L/min) ($q_{209}-q_{220}$)	ΔQ_{sp} (L/min) ($Q_{209}-Q_{220}$)	ratio _{sp} ($\Delta q_{sp}/(\Delta Q_{sp}-\Delta q_{sp})$)
10 MPa	2.44	9.10	36.64 %
15 MPa	2.81	9.50	42.00 %
20 MPa	3.80	10.90	53.52 %

the shaft direction, the larger the area of the SVPP and slipper pair oil film under the same pressure, the greater the carrying capacity, and the thicker the oil film generated by the hydrostatic effect, consequently the leakage increases. According to the structure, the SVPP and slipper pair oil film carrying areas are 9400 mm² and 24200 mm² respectively, with an area ratio of approximately 38.84 %. The similarity of the ratio_{sp} in Table 5 to the area ratio reflects the fact that the leakage of the slipper pair is greater than that of SVPP and qualitatively verifies the validity of the leakage model.

The growing relationship between SVPP leakage and total leakage at

Table 6

Contribution of leakage gap at variation pressure.

A			B				
	Δq_p (L/min)	ΔQ_p (L/min)	$\Delta q_p / \Delta Q_p$		Δq_p (L/min)	ΔQ_p (L/min)	$\Delta q_p / \Delta Q_p$
10 ~ 15 MPa	1.66	3.80	43.68 %		1.29	3.40	37.94 %
15 ~ 20 MPa	3.17	5.10	62.16 %		2.18	3.70	58.92 %

different pressures was analyzed. Fig. 18 was processed to obtain the SVPP leakage gap (Δq_p) and the total leakage gap (ΔQ_p) for pump A and pump B due to load pressure changes, as shown in Table 6.

The ratio ($\Delta q_p / \Delta Q_p$) reflects the gain of SVPP leakage to the total leakage growth, which is approximately 37.94 %~62.16 %. Both the increase in pressure and the decrease in spring stiffness enhance the SVPP's contribution to total leakage growth. The former effect is caused by the pressurized oil in the piston chamber directly offering hydrostatic support to the SVPP, and the damping holes in the slipper weaken the hydrostatic effect. This gap in effect is magnified at high pressures. The latter is due to the spring compressing the SVPP and the slipper pair in different directions, thus the force has a different sealing effect on the oil film, as can be understood from Eqs. (15)~(18). A similar effect can be seen in [55].

5. Conclusions

Leakage of the valve plate pair is one of the key factors affecting the pumps' volumetric efficiency, especially for the pumps with a specific SVPP structure and large displacement. In this paper, an accurate leakage model is obtained based on the cylinder block dynamics and the spherical oil film lubrication theories. Model results are verified through the actual pump experiments. The following conclusions can be drawn:

- (1) the increase in speed and load pressure both increase SVPP leakage, and they affect the oil film shape by varying the inertial force and hydraulic force of the block, respectively.
- (2) the central spring stiffness affects the Z-axis force and X-axis moment of the SVPP. A smaller stiffness deteriorates the tilt behavior of the CCB, with increased leakage and metal contact. A larger stiffness provides a beneficial effect on SVPP, but such enhancement is limited.
- (3) leakage from SVPP accounts for 20 %~30 % of the total leakage in the pump. About 37.94 %~58.92 % of the increase in total leakage caused by pressure changes comes from SVPP, and a decrease in central spring stiffness will further increase this percentage. Spring stiffness adjustment of $\pm 5\%$ can cause a maximum of 237 % leakage gap in simulation. Therefore, proper central spring stiffness should be maintained in the pump design and operation.

Declaration of Competing Interest

The authors declare that they have no known competing financial interests or personal relationships that could have appeared to influence the work reported in this paper.

Acknowledgments

This work was supported by the National Key Research and Development Program of China [Grant No. 2020YFB2007100]; the Major 2021 of science and technology in Hunan province-top 10 key technology projects [Grant No. 2021GK1070]; Changsha Science and Technology Plan Project [Grant No. KH2003025]; the Project of State Key Laboratory of Precision Manufacturing for Extreme Service Performance [Grant No. ZZYJKT2021-16]; Postgraduate Scientific Research Innovation Project of Hunan Province [Grant No. CX20220262]; and the

Fundamental Research Funds for the Central Universities of Central South University [Grant No. 2022ZZTS0176].

References

- [1] P. Ying, H. Tang, S. Ye, Y. Ren, J. Xiang, A. Kumar, Dynamic modelling of swashplate with local defects in axial piston pump and coupled vibration analysis, 110081, Mech. Syst. Signal Process. 189 (2023), <https://doi.org/10.1016/j.ymssp.2022.110081>.
- [2] J. Zhang, B. Liu, R. Lü, Q. Yang, Q. Dai, Study on oil film characteristics of piston-cylinder pair of ultra-high pressure axial piston pump, Process 8 (1) (2020) 68.
- [3] T. Wang, J. Fang, H. Liu, L. Chen, X. Ouyang, S. Guo, X. Zhao, Y. Lu, Modeling and characteristic analysis of a cylinder block/valve plate interface oil film model for 35 MPa aviation piston pumps, Machines 10 (12) (2022) 1196.
- [4] J. Zhou, J. Zhou, C. Jing, Experimental research on the dynamic lubricating performance of slipper/swash plate interface in axial piston pumps, Chin. J. Mech. Eng. 33 (2020) 25, <https://doi.org/10.1186/s10033-020-00441-7>.
- [5] X. Zhang, H. Wu, C. Chen, D. Wang, S. Li, Oil film lubrication state analysis of piston pair in piston pump based on coupling characteristics of the fluid thermal structure, 106521, Eng. Fail. Anal. 140 (2022), <https://doi.org/10.1016/j.engfailanal.2022.106521>.
- [6] G. Haidak, X. Wei, F. Li, A. Larbi, D. Wang, Heat effects modelling on the efficiency loss of the lubricating interface between piston and cylinder in axial piston pumps, 107846, Tribol. Int. 175 (2022), <https://doi.org/10.1016/j.triboint.2022.107846>.
- [7] J. Zhao, Y. Fu, J. Ma, F. Qu, Q. Chao, Y. Wang, Review of cylinder block/valve plate interface in axial piston pumps: Theoretical models, experimental investigations, and optimal design, Chin. J. Aeronaut. 34 (2021) 111–134, <https://doi.org/10.1016/j.cja.2020.09.030>.
- [8] Q. Chao, J. Zhang, B. Xu, H. Huang, M. Pan, A Review of High-Speed Electro-Hydrostatic Actuator Pumps in Aerospace Applications: Challenges and Solutions, J. Mech. Des. 141 (2019), <https://doi.org/10.1115/1.4041582>.
- [9] R. Ivantsyn, A. Shorbagy, J. Weber, An Approach to Visualize Lifetime Limiting Factors in the Cylinder Block/Valve Plate Gap in Axial Piston Pumps, in: ASME/BATH 2017 Symposium on Fluid Power and Motion Control, American Society of Mechanical Engineers, Sarasota, Florida, USA, 2017: p. V001T01A064. <https://doi.org/10.1115/FPMC2017-4327>.
- [10] T. Zlot, Simulation of the Hydrostatic Load of the Valve Plate-cylinder Block System in an Axial Piston Pump, Procedia Eng. 177 (2017) 247–254, <https://doi.org/10.1016/j.proeng.2017.02.196>.
- [11] U. Wieczorek, M. Ivantsynova, Computer aided optimization of bearing and sealing gaps in hydrostatic machines—the simulation tool CASPAR, Int. J. Fluid. Power 3 (2002) 7–20, <https://doi.org/10.1080/14399776.2002.10781124>.
- [12] H. Deng, L. Wang, Y. Guo, Y. Zhang, C. Wang, Analysis of the Hydrodynamic Lubrication Characteristics of the External Return Spherical Bearing Pair of an Axial Piston Pump/Motor, Math. Probl. Eng. 2020 (2020) e4902927. <https://doi.org/10.1155/2020/4902927>.
- [13] M. Ivantsynova, J. Grabbel, J.-C. Ossyra, Prediction of swash plate moment using the simulation tool CASPAR, in: Am Soc Mech Eng Digit Collect, 2008: pp. 1–9. <https://doi.org/10.1115/IMECE2002-39322>.
- [14] Q. Chao, J. Zhang, B. Xu, Q. Wang, Discussion on the Reynolds equation for the slipper bearing modeling in axial piston pumps, Tribol. Int. 118 (2018) 140–147, <https://doi.org/10.1016/j.triboint.2017.09.027>.
- [15] H. Yan, Y. Ren, L. Yao, L. Dong, Analysis of the internal characteristics of a deflector jet servo valve, Chin. J. Mech. Eng. 32 (2019) 31, <https://doi.org/10.1186/s10033-019-0345-7>.
- [16] J.-H. Shin, K.-W. Kim, Effect of surface non-flatness on the lubrication characteristics in the valve part of a swash-plate type axial piston pump, Mecc. 49 (2014) 1275–1295, <https://doi.org/10.1007/s11012-014-9893-1>.
- [17] H. Pan, J. Sheng, Y. Lu, Finite difference computation of valve plate fluid film flows in axial piston machines, Int. J. Mech. Sci. 31 (1989) 779–791, [https://doi.org/10.1016/0020-7403\(89\)90044-1](https://doi.org/10.1016/0020-7403(89)90044-1).
- [18] Z. Wang, Y. Xu, S. Hu, H. Ji, J. Yang, Research on lubrication mechanism with fluid-solid coupling of port plate pair in swash plate axial piston pump, Proc. Inst. Mech. Eng., Part J: Eng. Tribol. 234 (2020) 515–527, <https://doi.org/10.1177/1350650119872888>.
- [19] Z. Wang, S. Hu, H. Ji, Z. Wang, X. Liu, Analysis of lubricating characteristics of valve plate pair of a piston pump, Tribol. Int. 126 (2018) 49–64, <https://doi.org/10.1016/j.triboint.2018.05.008>.
- [20] M. Ivantsynova, C. Huang, Investigation of the Gap Flow in Displacement Machines Considering Elastohydrodynamic Effect, Proc. JFPS Int. Symp. Fluid Power. 2002 (2002) 219–229, <https://doi.org/10.5739/isfp.2002.219>.
- [21] S. Nie, M. Guo, F. Yin, H. Ji, Z. Ma, Z. Hu, X. Zhou, Research on fluid-structure interaction for piston/cylinder tribopair of seawater hydraulic axial piston pump in

- deep-sea environment, 108222, Ocean Eng. 219 (2021), <https://doi.org/10.1016/j.oceaneng.2020.108222>.
- [22] J. Jihai, Y. Weipeng, An approach to predict wear distribution of valve plate in elasto-hydrodynamic lubrication, IEEE Access. 7 (2019) 86789–86797, <https://doi.org/10.1109/ACCESS.2019.2923545>.
- [23] H. Tang, Y. Ren, J. Xiang, A novel model for predicting thermoelastohydrodynamic lubrication characteristics of slipper pair in axial piston pump, Int. J. Mech. Sci. 124–125 (2017) 109–121, <https://doi.org/10.1016/j.ijmecsci.2017.03.010>.
- [24] Y. Li, Z. Ji, L. Yang, P. Zhang, B. Xu, J. Zhang, Thermal-fluid-structure coupling analysis for valve plate friction pair of axial piston pump in electrohydrostatic actuator (EHA) of aircraft, Appl. Math. Model. 47 (2017) 839–858, <https://doi.org/10.1016/j.apm.2016.08.015>.
- [25] S. Hashemi, H. Friedrich, L. Bobach, D. Bartel, Validation of a thermal elastohydrodynamic multibody dynamics model of the slipper pad by friction force measurement in the axial piston pump, Tribol. Int. 115 (2017) 319–337, <https://doi.org/10.1016/j.triboint.2017.05.013>.
- [26] A. Schenk, M. Ivantsynova, A Transient Thermoelastohydrodynamic Lubrication Model for the Slipper/Swashplate in Axial Piston Machines, J. Tribol. 137 (2015), <https://doi.org/10.1115/1.4029674>.
- [27] S. Mukherjee, L. Shang, A. Vacca, A fast approach for coupled fluid-thermal modeling of the lubricating interfaces of axial piston machines, in: 12th Int Fluid Power Conf, 2020: pp. 327–340. <https://core.ac.uk/reader/353950440> (accessed February 28, 2023).
- [28] J. Zhang, Q. Chao, B. Xu, Analysis of the cylinder block tilting inertia moment and its effect on the performance of high-speed electro-hydrostatic actuator pumps of aircraft, Chin. J. Aeronaut. 31 (2018) 169–177, <https://doi.org/10.1016/j.cja.2017.02.010>.
- [29] D. Richardson, F. Sadeghi, R.G. Rateick, S. Rowan, Experimental and analytical investigation of floating valve plate motion in an axial piston pump, Tribol. Trans. 60 (3) (2017) 537–547.
- [30] S. Wegner, S. Gels, D.S. Jang, H. Murrenhoff, Experimental investigation of the cylinder block movement in an axial piston machine, Am. Soc. Mech. Eng. Digit. Collect. (2016), <https://doi.org/10.1115/FPMC2015-9529>.
- [31] J. Zhang, H. Xu, J. Chen, W. Huang, X. Huang, F. Lyu, B. Xu, M. Pan, Q. Su, Modeling and analysis of the tilt behavior of the cylinder block in a high-speed axial piston pump, 104735, Mech. Mach. Theor. 170 (2022), <https://doi.org/10.1016/j.mechmachtheory.2022.104735>.
- [32] J.M. Bergada, D.L. Davies, S. Kumar, J. Watton, The effect of oil pressure and temperature on barrel film thickness and barrel dynamics of an axial piston pump, Mecc. 47 (2012) 639–654, <https://doi.org/10.1007/s11012-011-9472-7>.
- [33] H. Xu, J. Zhang, G. Sun, W. Huang, X. Huang, F. Lyu, B. Xu, Q. Su, The direct measurement of the cylinder block dynamic characteristics based on a non-contact method in an axial piston pump, 108279, Measurement 167 (2021), <https://doi.org/10.1016/j.measurement.2020.108279>.
- [34] Z. Li, S. Xu, G. Gong, Y. Bi, L. Xu, L. Zhang, Z. Ren, Study on friction characteristics of slipper pair of large displacement high-pressure piston pump, Lubr. 10 (12) (2022) 363.
- [35] M. Khalil, On the dynamics of swash plate axial piston pumps with conical cylinder blocks, in: Canada Sherbrooke, 2001: p. 7.
- [36] M.K.B. Khalil, J.V. Svoboda, R.B. Bhat, Dynamic loads on the drive shaft bearings of a swash plate axial piston pump with conical cylinder block, Trans. Can. Soc. Mech. Eng. 27 (2004) 309–318, <https://doi.org/10.1139/tcsme-2003-0017>.
- [37] S.A. Kassem, M.K. Bahr, in: Current Advances in Mechanical Design and Production VII, Elsevier, 2000, pp. 139–148.
- [38] M.K.B. Khalil, J. Svoboda, R.B. Bhat, Modeling of swash plate axial piston pumps with conical cylinder blocks, J. Mech. Des. 126 (2004) 196–200, <https://doi.org/10.1115/1.1640363>.
- [39] S.A. Kassem, M.K. Bahr, Fuzzy logic control of constant power regulated swash plate axial piston pumps, in, Am. Soc. Mech. Eng. Digit. Collect. (2021) 125–133, <https://doi.org/10.1115/IMECE2001/FPST-25014>.
- [40] M.K. Bahr Khalil, J. Svoboda, R.B. Bhat, Experimental investigation on swash plate axial piston pumps with conical cylinder blocks using fuzzy logic control, Am. Soc. Mech. Eng. Digit. Collect. (2008) 11–18, <https://doi.org/10.1115/IMECE2002-39325>.
- [41] M.K. Bahr, J. Svoboda, R.B. Bhat, Vibration analysis of constant power regulated swash plate axial piston pumps, J. Sound Vib. 259 (5) (2003) 1225–1236.
- [42] Z. Shi, G. Parker, J. Granstrom, Kinematic analysis of a swash-plate controlled variable displacement axial-piston pump with a conical barrel assembly, 011002, J. Dyn. Syst. Meas. Control. 132 (2010), <https://doi.org/10.1115/1.4000067>.
- [43] L. Li, M.H. Xu, J. Ke, L.Y. Yu, Flow characteristic of axial piston pump with conical cylinder block, Appl. Mech. Mater. 42 (2011) 43–47, <https://doi.org/10.4028/www.scientific.net/AMM.42.43>.
- [44] Y.Q. Chen, Y.S. Wang, Calculating method for the leakage between slipper and swashplate in spherical swashplate type axial piston pump with conical cylinder, Adv. Mater. Res. 753–755 (2013) 2736–2741, <https://doi.org/10.4028/www.scientific.net/AMR.753-755.2736>.
- [45] B. Zhao, W. Guo, L. Quan, Cavitation of a submerged jet at the spherical valve plate/cylinder block interface for axial piston pump, Chin. J. Mech. Eng. 33 (2020) 67, <https://doi.org/10.1186/s10033-020-00486-8>.
- [46] J.M. Bergada, J. Watton, S. Kumar, Pressure, flow, force, and torque between the barrel and port plate in an axial piston pump, 011011, J. Dyn. Syst. Meas. Control. 130 (2008), <https://doi.org/10.1115/1.2807183>.
- [47] J.M. Bergada, S. Kumar, D. Li, J.W. Davies, A complete analysis of axial piston pump leakage and output flow ripples, Appl. Math. Model. 36 (2012) 1731–1751, <https://doi.org/10.1016/j.apm.2011.09.016>.
- [48] S. Kumar, J.M. Bergada, The effect of piston grooves performance in an axial piston pumps via CFD analysis, Int. J. Mech. Sci. 66 (2013) 168–179, <https://doi.org/10.1016/j.ijmecsci.2012.11.005>.
- [49] A. Shorbagy, R. Ivantsyn, J. Weber, An experimental approach to simultaneously measure the temperature field and fluid film thickness in the cylinder block/valve plate gap of an axial piston pump, Turbul. Heat Transf. 9 (2018) 863–875, <https://doi.org/10.1615/THMT-18.920>.
- [50] L. Qing, L. Gu, Y. Wang, Z. Lei, Analysis of leakage characteristics for bent-axis piston pump based on elastohydrodynamic deformation, Ind. Lubr. Tribol. 74 (2021) 18–25, <https://doi.org/10.1108/ILT-07-2021-0282>.
- [51] F. Lyu, J. Zhang, G. Sun, B. Xu, M. Pan, X. Huang, H. Xu, Research on wear prediction of piston/cylinder pair in axial piston pumps, 203338, Wear 456–457 (2020), <https://doi.org/10.1016/j.wear.2020.203338>.
- [52] A. Yamaguchi, Formation of a Fluid Film between a Valve Plate and a Cylinder Block of Piston Pumps and Motors : 2nd Report, A Valve Plate with Hydrostatic Pads : Heat Transfer, Combustion, Power, Thermophysical Properties, JSME Int. J. 30 (1987) 87–92, <https://doi.org/10.1299/jsme1987.30.87>.
- [53] J.M. Bergada, J. Watton, J.M. Haynes, D.L. Davies, The hydrostatic/hydrodynamic behaviour of an axial piston pump slipper with multiple lands, Mecc. 45 (2010) 585–602, <https://doi.org/10.1007/s11012-009-9277-0>.
- [54] J.M. Bergada, J.M. Haynes, J. Watton, Leakage and Groove Pressure of an Axial Piston Pump Slipper with Multiple Lands, Tribol. Trans. 51 (2008) 469–482, <https://doi.org/10.1080/10402000802044332>.
- [55] K. Ma, D. Wu, R. Xu, H. Pang, Y. Liu, Experimental investigation and theoretical evaluation on the leakage mechanisms of seawater hydraulic axial piston pump under sea depth circumstance, 106848, Eng. Fail. Anal. 142 (2022), <https://doi.org/10.1016/j.englfailanal.2022.106848>.